Focal mechanisms of the Lushan earthquake sequence and spatial variation of the stress field

LUO Yan[1]*, ZHAO Li[2], ZENG XiangFang[3] & GAO Yuan[1]

[1] *Institute of Earthquake Science, China Earthquake Administration, Beijing 100036, China;*
[2] *Institute of Earth Sciences, Academia Sinica, Taipei 11529, China;*
[3] *Key Laboratory of Computational Geodynamics, Chinese Academy of Sciences, Beijing 100049, China*

Using broadband seismic records from regional networks, we determined the focal mechanisms and depths of 37 earthquakes in the 2013 M7.0 Lushan earthquake sequence ($3.4 \leqslant M_w \leqslant 5.1$) by fitting the three-component waveform data. The results show that the earthquakes are predominantly thrust events, with occasional strike-slip mechanisms. Most earthquakes occurred at depths of 10–20 km. We derived the regional distribution of the average stress field in this area using the damped linear inversion method and the focal mechanisms obtained in this study. The inversion results suggest that the Lushan region and the adjacent area are mostly under compression. The orientations of the maximum principal axes trend NW-SE, with some local differences in the stress distribution at different depths. Compared with the distribution of the stress field in the Wenchuan earthquake area, the stress field in the southwest section of the Longmenshan Fault zone (LFZ) share similar characteristics, predominantly thrust faulting with a few strike-slip events and the maximum compression axes being perpendicular to the LFZ.

The Longmenshan Fault zone (LFZ) is located in the eastern margin of the Tibetan Plateau. Because of the eastward movement of the Tibetan Plateau as a result of the collision between the Indian and Eurasian Plates modified by the resistance of the rigid South China Block, strain energy in the region has been accumulating for a long time (Zhang et al., 2009; Royden et al., 2008). Numerical simulation suggests that the bottom of the upper crust in the entire LFZ is a high stress-growth area (Liu et al., 2012).

The M_w8 Wenchuan earthquake on 12 May, 2008 created a 300 km rupture along most of the northeast-striking Longmenshan thrust belt. The southwest segment of the

fault zone, over a length of 100 km, experienced relatively small movement and aftershocks were almost absent, indicating that in the Lushan area the accumulated strain energy had not been released. The Wenchuan earthquake had a great impact on the faults around the LFZ. According to the Coulomb stress change computed for models of perfect elasticity and viscoelasticity (Shan et al., 2009; Shao et al., 2010; Shi and Cao, 2010) the increment of the Coulomb stress in the southern segment of the LFZ is about 0.01 MPa. The results of the *in-situ* stress measurements in the southern segment of the LFZ (Qin et al., 2013) also show that the maximum principal stress in this area reached the critical value, and the fault may be at a critical stage. Generally speaking, earthquakes are triggered when the crustal stress exceeds the limits of the rock strength, causing a rapid

*Corresponding author (email: luoyan.wind@gmail.com)

release of strain energy and rupturing the fault zone. Following the long period of strain accumulation and after the strain release during the earthquake, crustal stress will adjust to reach a new balance. The Lushan earthquake may may be triggered by fault movement caused by the shear stress on the seismogenic fault exceeding the critical value.

Tectonic stress is the direct cause of earthquakes. Large earthquakes are manifestations of sudden releases of tectonic strain energy accumulated over time (Zhang et al., 2009). The focal mechanism of an earthquake reflects the regional stress field, thus providing a basis for studying tectonic stress. Focal mechanisms also provide constraints on the tectonic stress in the region surrounding the earthquake source. Various techniques for solving the unique stress field using earthquake focal mechanisms have been developed (McKenzie, 1969; Angelier, 1979, 1984; Gephart and Forsyth, 1984; Michael, 1984, 1987). Recently, Hardebeck and Michael (2006) introduced damping parameters into the linear stress inversion with bootstrapping (LSIB) approach of Michael (1984, 1987) so that the spatial-temporal variation of the stress field can be incorporated into the solution.

On 20 April, 2013 a magnitude 7.0 earthquake occurred at the LFZ (hereinafter the "Lushan earthquake"). The seismicity in this region was extremely weak without earthquakes above *M*6.5 and only two earthquakes above *M*6.0 (*M*6.0 on 12 June, 1941 and *M*6.2 on 24 February, 1970). Previous studies in this area focused on its tectonic evolution and present crustal deformation. With the increase in the number of digital seismic waveform records, it is necessary to conduct a full analysis of the seismic data to shed more light on the tectonic environment and evolution of this region from a seismological perspective. The main shock of the Lushan earthquake sequence was followed by a large number of aftershocks. Many broadband seismic instruments with good azimuth coverage were deployed in this area, and a large number of good-quality digital waveforms were recorded and can be used to study the spatial-temporal stress field in the southern segment of the LFZ.

In this study, we first collected the regional broadband waveforms recorded at the seismic stations in Sichuan Province. We then determined the focal mechanisms of 37 earthquakes of the Lushan earthquake sequence, including fault-plane solutions, focal depths, and moment magnitudes. Finally, we derived the distribution of the stress field in this region from the focal mechanisms by applying the Damped Linear Stress Inversion (DLSI) method (Hardebeck and Michael, 2006).

1 Earthquake focal mechanisms

Various methods have been developed to determine the focal mechanisms of earthquakes (Patton and Zandt, 1991; Dreger and Helmberger, 1993; Romanowicz et al., 1993;

Zhao and Helmberger, 1994; Zhu and Helmberger, 1996; Herrmann et al., 2011). Recently, an improvement on the Cut and Paste (CAP) method, the CAPJoint method, combined local Pnl, surface waveforms, and teleseismic P and SH waveforms to study earthquake source parameters (Chen et al., 2012). The CAPtele method has also been used to determine source parameters and to validate the reliability of the regional CAP method using teleseismic depth phases (Chen et al., 2012, 2013; Zhan et al., 2012).

In this study, we use the CAP method introduced by Zhao and Helmberger (1994) and improved by Zhu and Helmberger (1996). The CAP method adopts a grid search procedure to find the best double-couple fault-plane solution, moment magnitude, and focal depth of an earthquake by fitting the three components of the local and regional waveforms. In the algorithm, the three-component seismic waveform records are segmented into five windowed traces including two Pnl wave traces on the vertical and radial components and three S wave traces on the vertical, radial, and transverse components. The synthetic seismograms are computed using the frequency-wavenumber method (Zhu and Rivera, 2002) with a one-dimensional (1D) earth model, segmented into the same five traces as the observed waveform records. The Pnl and S waveform traces are bandpass filtered in different frequency bands with the Pnl filter having a slightly shorter period, and appropriate weights are assigned to the Pnl and S waves so that the final focal mechanism solution is not dominated by the much stronger S waves. The match between the recorded and synthetic waveforms is measured by cross-correlation, and a time shift is allowed between each pair of recorded and synthetic traces to account for the possible travel time anomaly caused by errors in the event location and origin time and the 3D heterogeneity inside the Earth. The enhanced contribution by the Pnl waves helps improve the resolution to the focal depth. The sPmP (or sPg) and sPn phases within the Pnl wave are sensitive to the source depth, and the relative strength between Pnl and the surface waves also puts a constraint on the source depth.

In recent years some achievements have been made using this method in China (Zheng et al., 2009; Luo et al., 2010; Luo et al., 2011; Zeng et al., 2013; Zhao et al., 2013).

Here, we use the CAP method to determine the earthquake focal mechanisms and depths of the Lushan earthquake sequence. The earthquake catalogs were provided by the China Earthquake Networks Center, and the waveform records are from the stations of the Sichuan Provincial Regional Seismic Network. In practice, we selected the phases used in the CAP solution based on the magnitude. For magnitude 4 earthquakes, we used P waves within an epicentral distance of 100 km and S waves within 200 km, whereas for magnitude 5 earthquakes, we used P waves within a distance of 150 km and S waves within 300 km of the epicenter. Traces with a low signal-to-noise ratio were discarded. We deconvolved the instrument responses, removed the mean

and linear trends, and then rotated the horizontal components to the radial and transverse components. The focal mechanism inversion was conducted through an iterative process. After each iteration the traces with low cross-correlation coefficients between the recorded and synthetic waveforms were discarded. We set the thresholds of the cross-correlation coefficients to be 70%. The earthquake focal mechanisms are determined with a minimum of five stations and at least 20 waveform segments.

Figure 1 displays an example of the CAP solution for the 20 April 2013 earthquake. Figure 1(a) shows the 1D model used in this study, which is an average layered model (Zheng et al. 2009) of the LFZ region. It incorporates the features of the crustal structures of the Sichuan Basin to the east and the Tibetan Plateau to the west. Figure 1(b) shows the locations of the stations used in determining the earthquake focal mechanism of the M_w5.1 aftershock on 20 April, 2013. The waveform residuals of the best fault-plane solutions for all the trial focal depths are shown in Figure 1(c). The solution with the minimum waveform mismatch, considered to be the optimal solution, was the depth of 13 km. Figure 1(d) shows the waveform comparisons for the final focal mechanism solution. The inversion results suggest that the best double-couple solution of the earthquake is 221°, 51° and 90° for the strike, rake and dip, respectively, with a focal depth of 13 km.

We determined the focal mechanisms for a total of 37 earthquakes ($3.4 \leq M_w \leq 5.1$) using the CAP method. As shown in Figure 2, most of the focal mechanisms of the Lushan aftershocks display characteristics similar to those of the mainshock. Generally, the aftershocks are primarily thrust events distributed throughout the rupture zone. The thrust events dominate, albeit with a few strike-slip events (20130420：101905, 20130420：133635, 20130420：160602,
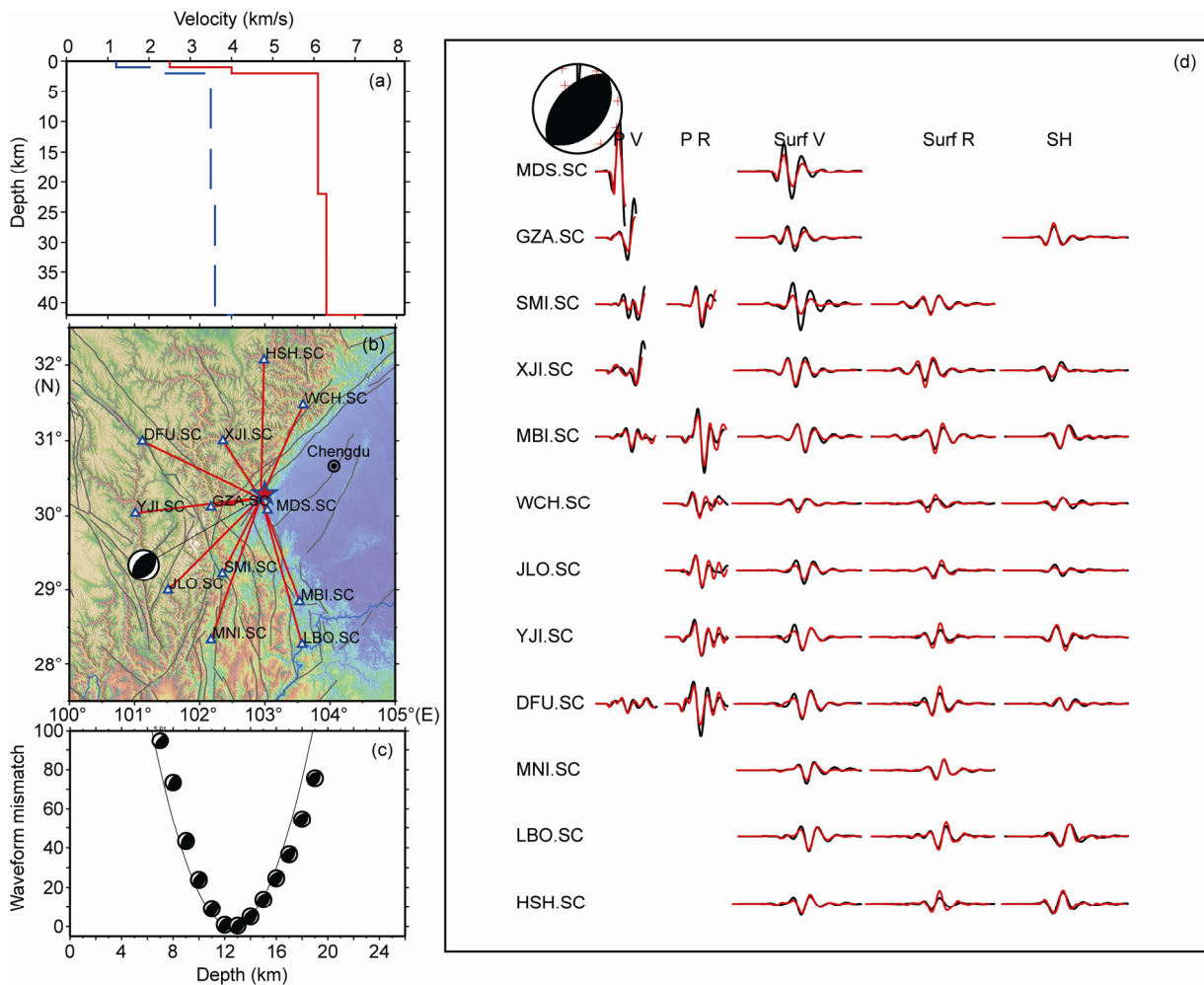
Figure 1 Example of focal mechanism inversion using the CAP method for the M_w5.1 aftershock that occurred at 11:34 on 20 April, 2013. (a) 1D layered model used for computing the synthetic seismograms. (b) Locations of stations used in the inversion. (c) The waveform mismatch of the best fault-plane solutions for all the trial focal depths; the 13-km depth with the minimum waveform residual is taken as the optimal focal depth. (d) Comparison of observed (black) and synthetic (red) waveforms at 12 stations. The waveform fit is evaluated independently for the maximum of five traces including the vertical and radial traces for P waves (PV, PR) and the vertical, radial, and transverse traces for S waves (SurfV, SurfR, SH). The left column lists station codes and at the top left is the beach ball (lower-hemisphere stereographic projection) of the fault-plane solution for the optical focal depth of 13 km.
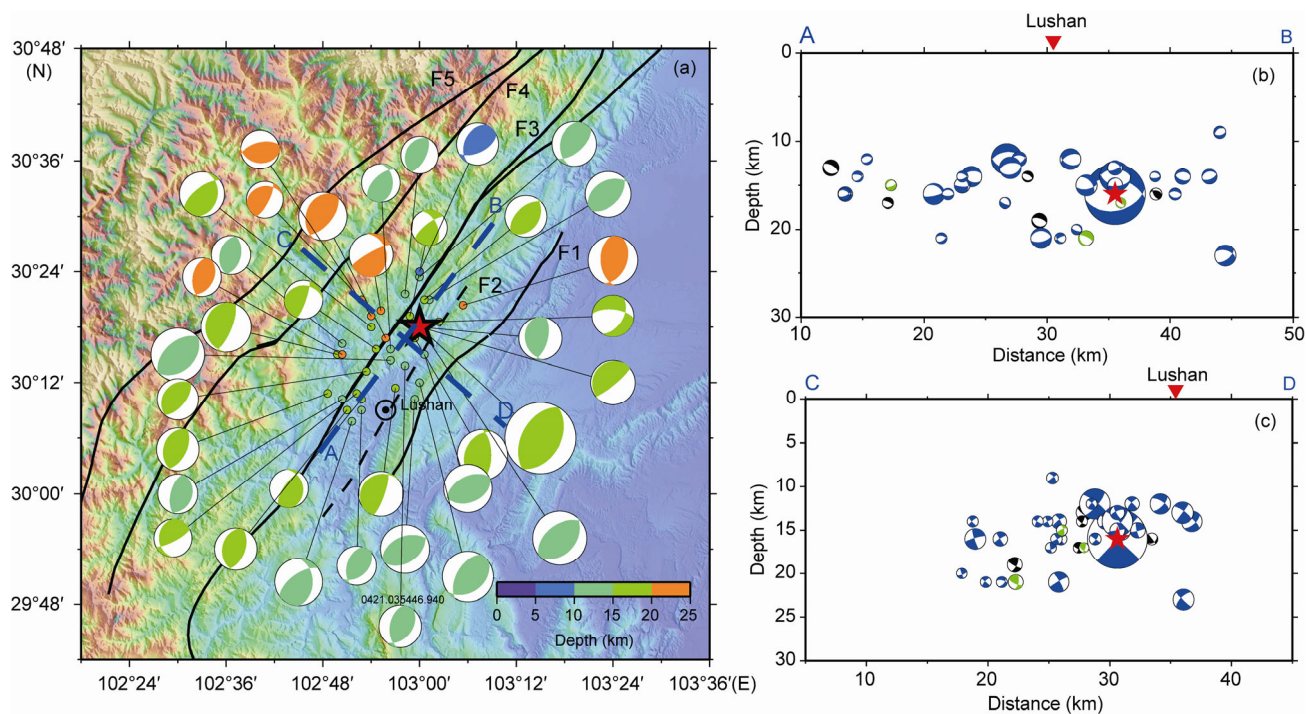
Figure 2   Beachball plots of 37 earthquakes (3.4≤M_w≤5.1) determined in this study. (a) Focal mechanisms distribution; size and color of the beachballs indicate the moment magnitude and source depth, respectively. The bold black lines represent faults. (b) Focal mechanisms in cross-sectional view along the AB section shown in (a). (c) Focal mechanisms in cross-sectional view along the CD section shown in (a). The size and color of the beachballs indicate the moment magnitude and source type, respectively. Blue indicates thrust events (55°≤rake≤125°), green represents strike slip events (−35°≤rake≤35°, or −180°≤rake≤−145°, or 145°≤rake≤180°), and black indicates mixed events (35°<rake<55°, or 125°<rake<145°, or −55°<rake<−35°, or −145°<rake<−125°).

with a strike/dip/rake of: 348°/31°/20°, 180°/28°/31°, 336°/53°/23°, respectively). There are five mixed events (20130420：174514, 20130420：144320, 20130420：093934, 20130421：170154, and 20130421:221655, with a strike/dip/rake of: 276°/63°/−46°, 348°/29°/47°, 0°/41°/44°, 360°/39°/52°, and 10°/31°/52°, respectively). As shown in Figure 3, most of the strikes of the aftershocks are in the range of 180°–210°, the dips are in the range of 70°–90°, and the rakes are 30°–60°. The dip angles of the thrust events are consistent with the geological survey result (Yang et al., 1999). The strike of event 20130420：155326 (strike/dip/rake of 56°/60°/79°and 21 km source depth) trends approximately E-W, perpendicular to the main rupture zone of the Wenchuan earthquake. This event may be a result of the stress adjustment of deep small faults in the source region triggered by the main shock. The 20130421：164538 event is a thrust event with a strike-slip component. One nodal plane of the fault-plane solution is strike-slip and the other is thrust with a dipping angle, which may be caused by the low-quality data. The strike/dip/rake of the two events of 20130420：091153 and 20130421：173027 is 181°/19°/70° and 210°/10°/70°, respectively, with dip angles less than 20°, displaying a low dip angle feature different from other events of this earthquake sequence. The other nodal planes are 22°/72°/96°, 50°/80°/93°, and 22°/72°/96°, which may be

thrust fault planes dipping southeastward with a high dip angle or dipping northwestward with a dip angle of about 45°.

The depth distribution of the events in Figure 2(b), (c) shows that most of the aftershocks occurred in the depth range of 10–20 km, with six events deeper than 20 km. The overall trend indicates that events that occurred east of the LFZ are shallower than those that occurred west of the LFZ, which may imply that the fault plane dips northwestward. The events in the north segments are deeper than those in the south, showing a distribution trend similar to that of the aftershocks. From a seismogenesis point of view, the depth distribution of the focal depths determined in this study suggests that the upper crust of the LFZ is brittle and can generate seismic events, while the deeper crust is in a state of ductile deformation and the accumulated strain energy is not sufficient to trigger earthquakes. Thus, the depth of the deepest earthquake can be considered the depth where the transition from a brittle regime to a ductile one occurs.

Figure 4 shows the horizontal projections of the *P* and *T* axes of the focal mechanisms. Most of the *P* axes (Figure 4(a)) are oriented NW-SE, perpendicular to the LFZ, and are nearly horizontal (plunge<35°) whereas the *T* axes (Figure 4(b)) are nearly vertical (plunge>55°). The events are mostly thrust earthquakes, with a few strike-slip earthquakes. This is consistent with the surface horizontal velocity field from GPS observations (Shen et al., 2005; Wang et
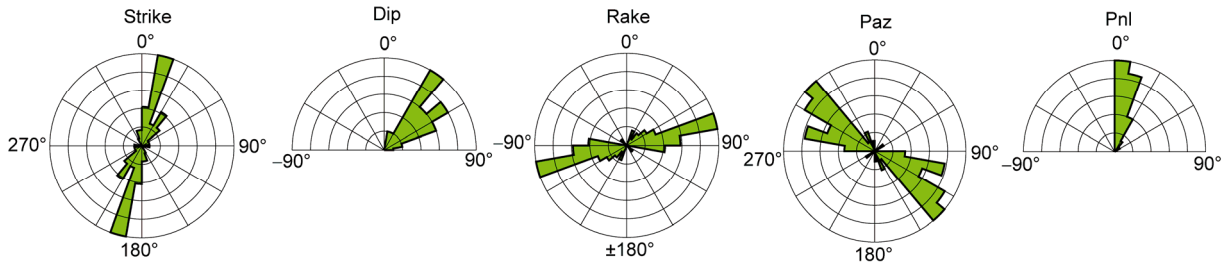
Figure 3   Rose maps of the strike, dip, and rake of the Lushan earthquake sequence.
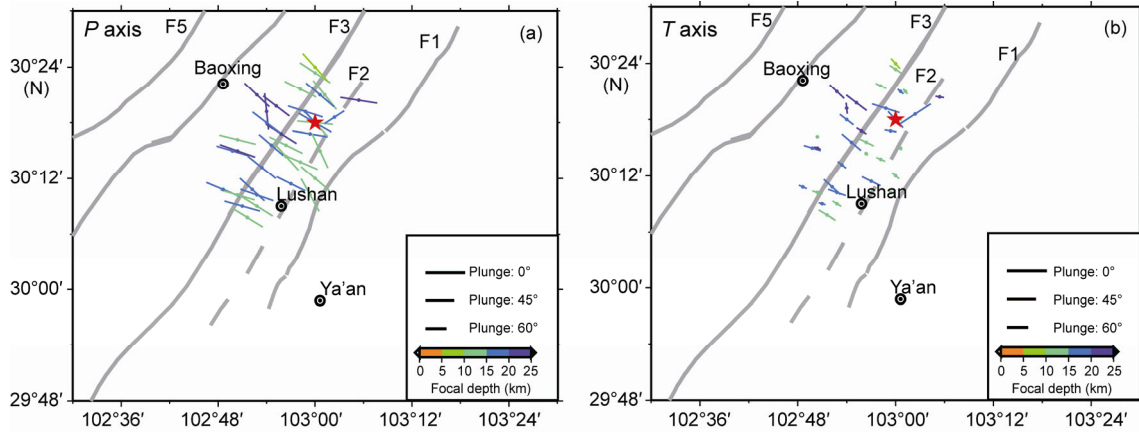
Figure 4   Horizontal projections of the *P* and *T* axis of the focal mechanisms. (a) Horizontal projections of the *P* axis. Circles indicate aftershocks, the lengths of the lines indicate the horizontal projection components of the *P* axis. The color of the lines indicates the focal depths, gray bold lines represent faults. (b) Horizontal projections of the *T* axis.

al., 2008; Zhang, 2013).

2 Spatial variation of the stress field

Earthquakes are caused by the buildup of regional stress in the crust over an extended period. Therefore, the focal mechanisms, i.e., the orientations of the *P*, *B*, and *T* axes, are closely linked to the stress field. However, the focal mechanism of an individual earthquake is also dependent on the geometry of the fault plane. Therefore, though there is usually no direct relation between the focal mechanism of a particular earthquake and the stress field (McKenzie, 1969), we can deduce the geometrical properties of the stress field from the collective behavior of many earthquakes in a region. Several techniques were developed to determine the spatially uniform stress field from the fault-plane solutions of a group of earthquakes (Angelier, 1979; Gephart and Forsyth, 1984; Michael, 1984, 1987). The variation of the stress field can be resolved by subdividing the earthquakes in space and time and solving for each subset separately.

Uniform stress field inversion is based on the assumption that the slip vector on the fault plane of an earthquake is parallel to the tangential traction. A linear relationship can be established between the components of the unit slip vector and the stress tensor elements. If the stress field is constant over a specific spatial-temporal range, then given a sufficient number of focal mechanisms we can invert for the stress tensor (Michael, 1984, 1987). Hardebeck and Michael (2006) introduced spatial and temporal damping parameters and developed the technique of damped regional-scale stress inversion (DRSSI). In their damped linear inverse problem, the stress field is a least-square solution of the equation

$$(\mathbf{G}^T\mathbf{G} + e^2\mathbf{D}^T\mathbf{D})\boldsymbol{m} = \mathbf{G}^T\boldsymbol{d}, \tag{1}$$

where $\boldsymbol{m}$ is the model vector containing the stress tensor elements at the grid points, $\boldsymbol{d}$ is the data vector that includes the slip vector components of the earthquakes at the corresponding grid points, and $\mathbf{G}$ is the data kernel matrix involving the normal vector components of all the fault planes. The damping matrix $\mathbf{D}$ is formed by blocks of zeros, the identity matrix $\mathbf{I}$, and its opposite $-\mathbf{I}$, and e is the damping parameter. The damping factor is chosen so as to achieve an optimal trade-off between the data error and the model size. Once the stress tensor elements are obtained on each grid point, we can solve for the eigenvectors to derive the orientations of the principal stress axes.

In this study, we used 37 focal mechanisms to determine the regional stress field around the Lushan region using the DRSSI method. Since the earthquakes we used occurred over a short time interval, we do not divide the earthquakes

in time; instead, we focus on inverting the focal mechanisms for spatial variation. After several trial inversions with different grid sizes, we selected a grid size of 0.05° in both latitude and longitude. Taking into account the earthquake location errors and the fact that each earthquake is influenced by the stress field in a certain area, for each grid point we assigned the earthquakes within a distance of 0.05°. Following the same approach as in Zhao et al. (2013), we determined the optimal damping factor *e* by first calculating the trade-off curve between the data error and model size (Figure 5(a)), and then found the maximum curvature of the trade-off curve (Figure 5(b)). The value of the optimal damping factor was found to be *e*=0.3 for the 0.05° grid. Larger grid spacing can retrieve the large-scale pattern of the stress field, but will mask some obvious small scale features. See Figure 6(a) for an example of a 0.2° grid in both longitude and latitude.

After obtaining the stress tensors at the grid points using the DRSSI, we obtain the principal stress axes at each grid point by calculating the eigenvalues and eigenvectors of the stress tensor. Figure 6(b) shows the 2D map of the stress field. The horizontal projections of the maximum and minimum principal axes σ_1 and σ_3 are shown for each grid point, respectively. The minimum principal stress axis σ_3 (minimum compression) is depicted with a hollow line segment, while the maximum principal stress axis σ_1 (maximum compression) is represented by a solid green or blue line segment according to the corresponding faulting type. A solid green line segment indicates strike-slip faulting with both σ_1 and σ_3 nearly horizontal (plunge<35°), whereas a solid blue line segment indicates thrust faulting with a nearly horizontal σ_1 and a nearly vertical σ_3 (plunge>55°). A solid gray line segment represents a mixed type that cannot be categorized as simple strike-slip, normal, or thrust.

The focal mechanism inversion results in Figure 6(b) show that around the Lushan region the tectonic stress field is predominantly in a thrust faulting environment with nearly horizontal maximum compression in the NW–SE direction and nearly vertical minimum compression. The

stress field also shows local spatial variation. In the northern part of the Lushan region the stress field environment displays strike-slip fault features. In southern Lushan the orientation of the maximum compression axes changes from NW, NNW to nearly EW. However, since the distribution of the earthquakes (circles in Figure 6(b)) is not adequate to constrain the stress field inversion, the inconsistent orientation may be caused by the lack of suitable data.

To study the stress environment at different depths, we divided the earthquakes into two groups: those with focal depths of 5–15 km and those with focal depths of 16–25 km. Figure 6(c) displays the horizontal projection of the maximum and minimum principal axes σ_1 and σ_3, respectively, at the depth range of 5–15 km, and Figure 6(d) shows the projections for depths of 16–25 km. Generally, the stress environment for both sets of focal depths are mainly thrust faulting with the orientations of the maximum compression axes primarily trending NW-SE, except for some local differences in the faulting style and orientation of the stress field. However, the number of earthquakes in those regions (circles in Figure 6) may not be sufficient for obtaining reliable average stress field results using our method. Therefore, the stress difference may be an artifact of inversion and more focal mechanism solutions are required to verify it.

3   Discussion

The steep terrain and strong velocity contrast across the Longmenshan fault affect the propagation of high-frequency seismic waves in this region (Li et al., 2011, 2012, 2013; Zheng et al., 2013). Low-pass filtering and time shifting between real and synthetic waveforms were applied to reduce the effects of heterogeneity. In this study, focal mechanisms of 37 earthquakes were obtained with the CAP method. The majority of the fault-plane solutions of the aftershocks are consistent with those of the main shock. The strike angles concentrate around 180°–210° while most of the aftershocks are thrust events. There are also a few thrust
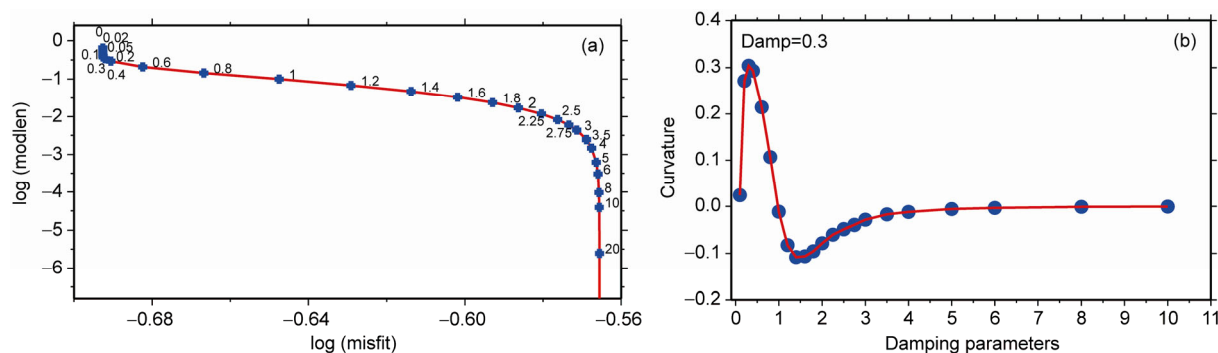
Figure 5   Determining the optimal damping factor. (a) Trade-off curve for the damped regional-scale stress inversion using the 37 fault-plane solutions in Figure 6(b). Crosses show the trade-off between the data misfit and model length for different values of the damping parameter *e*. From left to right along the trade-off curve, the damping parameter *e* runs from 0 to 20. (b) Curvature of the trade-off curve as a function of damping parameter *e*. The optimal damping parameter *e*=0.3 is chosen where the trade-off curve has the maximum curvature.
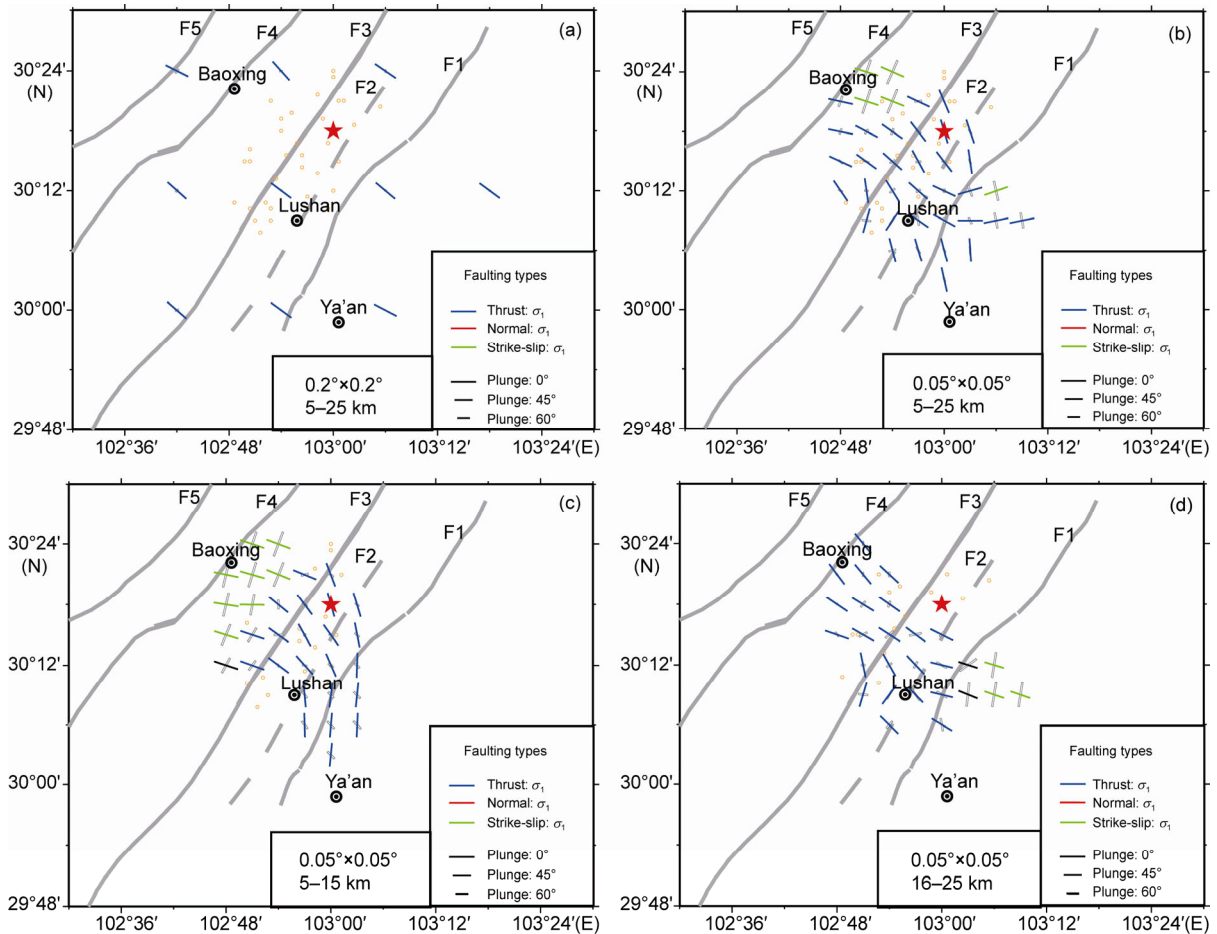
Figure 6 Results of stress field inversion from the 37 fault-plane solutions. Horizontal projections show the maximum principal stress axis σ_1 (maximum compression) and minimum principal stress axis σ_3 (minimum compression). Hollow gray line segments represent σ_3; blue, green, and black line segments represent σ_1, indicating thrust, strike-slip, and mixed faulting environments, respectively. (a) Larger grid spacing example (0.2° in both longitude and latitude). For the stress vector at each grid point, the earthquakes (yellow circles) within the 0.2° interval are included in the inversion. (b) Two-dimensional grid with uniform grid spacing of 0.05°, for events at depths of 5–25 km. (c) Same as in (b) but for depth range of 5–15 km. (d) Same as in (b) but for depth range of 16–25 km.

earthquakes with different strike or strike-slip angles. The variation of the focal mechanisms may be due to the complicated seismogenic fault system. The seismogenic fault system consists of a main detachment and several sub-faults at the hanging wall. The slip of the main detachment results in the failure of the sub-faults. There are parallel strike-slip sub-faults as well as several thrust sub-faults with different strike angles. The aftershocks with different focal mechanisms may have occurred on these thrust sub-faults.

Our results are consistent with previous studies of mainshock focal mechanism (Xie et al., 2013; Zeng et al., 2013). Lu et al. (2013) also used the CAP method to invert focal mechanisms of aftershocks. To compare these results we used the Kagan angle rotation method (Kagan, 1991). The Kagan Angle is defined as the angle between two slip vectors. A smaller Kagan Angle denotes a smaller difference between two focal mechanisms. The Kagan Angle of most of the aftershocks was less than 30° (Table 1). The larger differences in focal mechanisms of three of the events

may have been caused by a low signal-to-noise ratio.

An earthquake is the result of strain energy accumulation that is increased by tectonic stress loading. When the stress exceeds the strength of the rock, rock failure will release strain energy as an earthquake. Post-seismic changes in the stress field have been reported (Guo et al., 2009; Wu et al., 2010). During the 2008 Wenchuan earthquake the northern part of the Longmenshan Fault ruptured while the southern part was seismically inactive. The strain energy in the source region of the Lushan earthquake had not been released. The change of stress induced by the Wenchuan earthquake may have been up to 0.1 MPa (Parsons et al., 2008; Toda et al., 2008; Wan et al., 2009; Shan et al., 2009; Shao et al., 2010). *In-situ* stress measurements in 2003, 2008, and 2010 suggested that the stress in the southern part of the Longmenshan fault was still high (Qin et al., 2013). The maximum horizontal stress was observed close to the lower boundary of the failure in the southwest end of the Longmenshan Fault. Our results are consistent with the axis

Table 1   Comparison of our focal mechanism results and those of Lu et al. (2013)

origin time	Longitude (E)	Latitude (N)	Depth (km)	M_w	Strike/dip/rakd (°)	Depth (Lu) (km)	M_w (Lu)	Strike/dip/rake (Lu) (°)	KA (°)
20140420:080247	103.00°	30.30°	16	6.64	210/47/90	14	6.60	209/46/94	4.85
20140420:090258	102.93°	30.28°	21	4.56	199/31/72	18	4.40	186/19/81	24.61
20140420:091153	102.83°	30.25°	16	4.72	181/19/70	15	4.60	204/14/102	12.81
20140420:092010	102.99°	30.17°	14	4.59	55/44/81	12	4.50	228/42/94	17.09
20140420:092601	102.95°	30.19°	15	4.27	19/77/81	12	4.20	152/8/42	16.66
20140420:093729	102.99°	30.28°	15	4.71	360/61/77	12	4.60	357/72/80	12.09
20140420:093934	102.86°	30.13°	13	4.47	0/41/44	10	4.30	215/54/91	27.84
20140420:101905	102.92°	30.33°	21	4.15	348/31/20	17	4.00	245/60/124	20.48
20140420:102947	102.81°	30.18°	16	4.00	197/33/82	11	3.80	186/29/83	12.52
20140420:103836	103.01°	30.25°	12	4.54	241/50/84	10	4.40	213/50/92	33.69
20140420:113416	102.94°	30.24°	12	5.06	228/51/90	14	5.00	212/50/98	21.99
20140420:151833	103.00°	30.39°	14	4.16	191/37/58	10	4.00	219/33/104	28.12
20140420:155326	102.90°	30.32°	21	3.66	256/60/79	17	3.50	266/51/80	13.06
20140420:174514	103.04°	30.31°	16	3.92	276/63/–46	14	3.80	203/61/-159	87.00
20140420:185903	103.00°	30.40°	9	3.96	207/39/60	12	3.90	253/60/124	51.15
20140420:191250	103.02°	30.35°	14	4.32	43/50/78	11	4.20	242/31/129	26.63
20140421:001435	102.85°	30.15°	16	3.97	190/36/82	12	3.80	198/24/96	14.44
20140421:023207	103.01°	30.35°	16	3.95	32/37/78	10	3.80	232/30/114	26.61
20140421:035446	102.97°	30.23°	12	4.01	190/50/71	9	3.90	192/40/78	11.53
20140421:045345	103.09°	30.34°	23	4.68	177/49/73	16	4.50	200/30/106	27.96
20140421:092932	102.91°	30.26°	17	3.62	19/80/63	17	3.50	292/20/-171	16.04
20140421:115940	103.00°	30.20°	13	4.81	210/54/75	11	4.70	213/53/99	22.37
20140421:123918	102.89°	30.22°	16	3.87	39/61/90	13	3.70	238/22/134	28.81
20140421:170525	103.00°	30.30°	14	5.07	41/41/81	10	4.90	202/40/90	27.60
20140421:173027	103.00°	30.30°	15	4.21	210/10/70	9	4.10	174/21/62	30.34
20140421:184825	103.00°	30.30°	13	4.07	170/30/69	9	4.00	203/21/106	17.91
20140421:221655	102.90°	30.30°	19	4.22	10/31/52	16	4.10	247/57/121	16.14
20140421:232523	102.84°	30.25°	21	3.66	191/51/78	17	3.60	203/30/103	27.23

of maximum horizontal stress (Qin et al., 2013).

Our investigation of the tectonic features of the LFZ raised some important questions. What is the compressional stress axis? Is the stress field in the shallow crust consistent with that in the middle crust? We aim to answer these questions based on our results of the stress field after the Lushan earthquake.

The 2D inversion using the 0.05° grid shows that the stress field in Lushan is dominated by the thrust component. The axis of the maximum horizontal stress lies NW-SE. There are some local variations of the stress field. To the north of Baoxing, the dominant component is strike-slip while thrust dominates the stress field between Baoxing and Lushan. Although the dominant component of the stress field in the southern part of Lushan is thrust, the axis of the maximum horizontal stress shows a slight rotation, becoming NNW-SSW or N-S. The 3D inversion result also suggests that the stress field changes with depth. Since the centroid depth of the mainshock is 15 km, the main detachment may slip at the same depth. Thrust sheets in the hanging wall ruptured after the Lushan aftershock. To the west of the Shuangshi-Dachuang fault, the thrust sheets are NWW strike-slip rotating to NW. To the south of the Lushan blind

fault, the orientation changes to N-S. The ruptures beneath the main detachment occurred at secondary faults and have similar orientation. However, the resolution in the deeper part is limited by available data and more focal mechanisms are needed to verify this hypothesis.

We also inverted the focal mechanism solution of some of the Wenchuan earthquake's aftershocks and compared the stress field in the source regions of the Lushan and Wenchuan earthquakes. The southwestern part of the Longmenshan Fault was divided into four segments (Figure 7). The principal stress axes at each segment were inverted with the LSIB (Linear Stress Inversion with Bootstrapping) method (Michael, 1984, 1987). To reach 95% confidence interval, we ran 2000 inversions. In Figure 7, σ_1 was projected onto the horizontal plane and shown as a solid orange line. The three principal stress axes are projected onto the hemisphere and shown as colored dots. In segments A, B, and D, the stress field is dominated by thrust components. The maximum stress axis is almost horizontal while the minimum one is nearly vertical. The orientation of σ_1 is NW−SE which is perpendicular to the Longmengshan Fault whereas the axes of σ_1 in segments A, B, and D are a little different. The average σ_1s in segments A and B are different
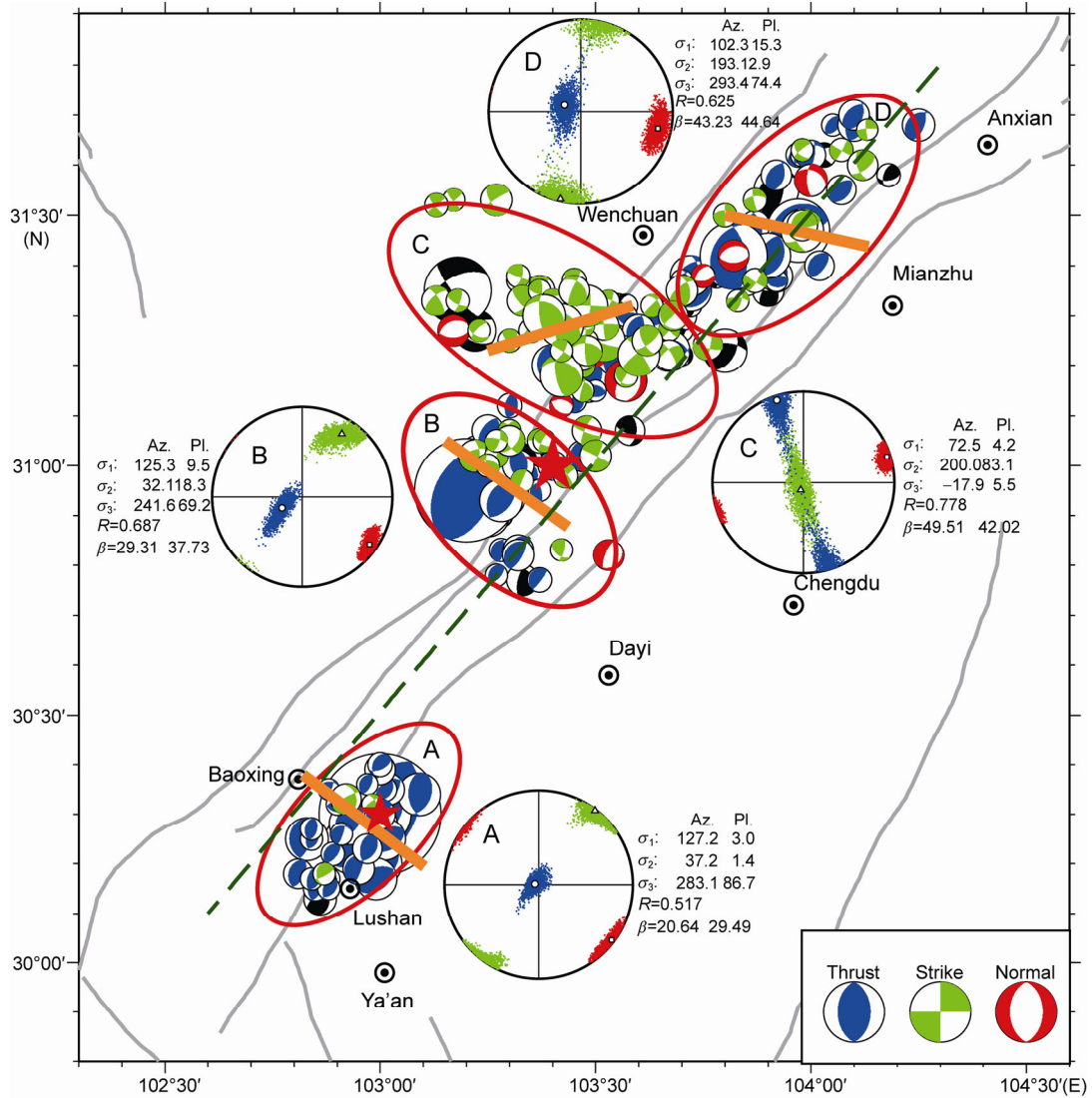
Figure 7 Average stress in the southwest segment of the LFZ. The study region is divided into four segments: A, B, C, and D, illustrated as ellipses, the bold orange lines represent the horizontal projection of the maximum compression axes of the average stress in each segment. The results of the LSIB inversion are displayed in circles next to the corresponding ellipse segments. Red indicates the maximum principal stress axes, blue represents the minimum principal stress axes, and green represents the middle axes.

from that in segment D. The plunge of σ_1 in segment D (15.3°) is much larger than in A (3.0°) and B (9.5°) while the orientation rotates from NE-SW to NWW-SE. The stress field in the Xiaoyudong Fault (segment C) shows a different pattern. The dominant component is strike-slip while the axis of σ_1 is NE-SW.

The primary stress field is defined as one controlled by compressional forces loading at plate boundaries. The Longmenshan Fault is the boundary between two primary stress fields in mainland China. The stress field in the Tibetan Plateau is predominantly a SSW-NNE compressional environment but the maximum compression stress shows a rotation at the eastern margin. From the north to south, the axis rotates from NE to SE (Xu, 2001; Xie et al., 2004). The collision between the Indian and Eurasia plates, which results in the uplift of the Tibetan Plateau, dominates the

stress field variation (Xu, 2001).

The east to southeastward movement of the Bayan Har block loads a perpendicular compression force on the Longmengshan Fault. With similar tectonic loading, different tectonic environments will lead to different stress fields. The stress field in the southwest segment has a similar SE compression stress as the primary stress field. The Xiaoyudong Fault was considered as a tear fault and accommodated different amounts of shortening in different segments of the Longmengshan Fault. Because the shortened amount of the southern segment of the Longmengshan Fault is much larger than that of the northern segment, this fault is a left-lateral slip fault as our focal mechanism solution shows. Due to strong compression in the southern Longmengshan Fault, the Xiaoyudong Fault also carries a compression component. Normal slip earthquakes may occur in this region at anti-

clines that rupture under compressional loading.

The stress field can be obtained from different datasets, such as focal mechanisms, in-situ stress measurements, and shear wave splitting. The focal mechanism dataset only samples the deeper part of the fault; therefore, it reflects the stress field of the middle crust. Combining earthquakes at different faults, the regional scale stress field, which is controlled by tectonic loading, could be inverted. The *in-situ* stress measurements reflect the stress field near the surface (<hundreds of meters). Different S phases can sample different parts of the crust. The splitting of the teleseismic phase is controlled by anisotropy of the uppermost mantle and the crust beneath station while the regional phase could sample the path between the station and the source. Xu et al. (2001) combined earthquake focal mechanisms and in-situ measurement and provided a stress map of East Asia. Xie et al. (2011) discussed the tectonic stress field of the eastern margin of the Tibetan Plateau based on the China mainland crust stress database. Both studies concluded that the axis of the maximum horizontal stress lies NW-SE. Dense sampling of the regional shear wave splitting enables the detection of small-scale heterogeneities in the stress field. Previous studies suggest that the axes of the maximum compressive stress beneath the MDS and L5503 stations lie NW-SE (Shi et al., 2009, 2013). A recent study also reveals the σ_1 rotated from a NW orientation to nearly E-W in the Lushan region (Gao et al., 2013). A teleseismic shear wave splitting study provided a similar result (Wang et al., 2007). In summary, both large- and small-scale stress field studies have shown that the NW-SE thrust component dominates the stress field in the southwestern Longmengshan Fault.

4 Conclusions

Using regional broadband waveform records from seismic stations in Sichuan province, we determined the focal mechanisms, focal depths, and moment magnitudes of 37 earthquakes in the Lushan earthquake sequence using the CAP method. The earthquakes are mainly thrust events and several are thrust events with a few strike-slip components (20140421：164538 and 20140420：101905) in the Lushan central section; the strikes are approximately in the NE direction, consistent with the LFZ. We also observed a thrust event (20140420：155326) with a strike perpendicular to the LFZ, which may have been triggered after the main shock by the stress adjusting around the source region. Most of the earthquakes occurred at depths of 10–20 km. The overall pattern is that events east of the LFZ are shallower than those west of the fault, suggesting a northwestward-dipping fault plane. The events in the northern section are deeper than those in the south, suggesting that the faults may be segmented.

After obtaining stable and reliable earthquake focal mechanisms, we calculated the 2D spatial variation of the stress field using the Damped Linear Stress Inversion method in two grid sizes: grid spacing of 0.2° and 0.05°, in both latitude and longitude. The larger-spaced grid of 0.2° can reflect the large-scale pattern of the stress field, but may conceal some obvious local features. The results with a grid size of 0.05° showed that the tectonic stress field is predominantly in a thrust faulting environment with a nearly horizontal maximum compression in the NW-SE direction and nearly vertical minimum compression, but shows spatial variations on a local scale. In the region around Baoxing, the stress environment occasionally has strike-slip faulting features, and the orientations of the maximum compression axes change from NW-SE to NNW-SSE. To study the stress environment at different depths, we divided the earthquakes into two groups based on the focal depths: 5–15 km (shallower group) and 16–25 km (deeper group). Both sets of stress fields retrieved from the two groups of focal mechanisms have primarily thrust-faulting features with the maximum compression axes at a NW-SE orientation, except for some local differences in the faulting type and stress field orientation.

Comparing the average stress fields between the Lushan earthquake source region and Wenchuan earthquake source region, the stress environment in the Lushan region is similar to that of the Wenchuan region, predominantly thrust fault type with nearly horizontal σ_1 and nearly vertical σ_3. The orientation of the maximum compression axes is NW-SE, approximately perpendicular to the LFZ.

Angelier J. 1979. Determination of the mean principal directions of stresses for a given fault population. Tectonophysics, 56: T17–T26

Angelier J. 1984. Tectonic analysis of fault slip data sets. J Geophys Res, 89: 5835–5848

Burchfiel B C, Royden L H, van der Hilst R D. 2008. A geological and geophysical context for the Wenchuan earthquake of 12 May 2008, Sichuan, People's Republic of China. GSA Today, 18: 4–11

Chen W W, Wang D, Wei S J. 2013. A study on the uncertainties of the centroid depth of the 2013 Lushan earthquake from teleseimic body wave data. Acta Seismol Sin-Engl Ed, 26: 161–168

Chen W W, Ni S D, Wang Z J, et a1. 2012. Joint inversion with both local and teleseismic waveforms for source parameters of the 2010 Kaohsiung earthquake (in Chinese). Chin J Geophys, 55: 2319–2328

Deng Q D, Chen G H, Zhu A L. 2011. Discussion of rupture mechanisms on the seismogenic fault of the 2008 M_s8.0 Wenchuan earthquake. Sci China Earth Sci, 54: 1360–1337

Dreger D, Helmberger D V. 1993. Determination of source parameters at regional distances 360 with single station or sparse network data. J Geophys Res, 98: 8107–8125

Gao Y, Wang Q, Zhao B, et al. 2014. A rupture blank zone in middle south part of Longmenshan Faults: Effect after Lushan M_s7.0 earthquake of

20 April 2013 in Sichuan, China. Sci China Earth Sci, 57: 2036–2044

Gephart J W, Forsyth D V. 1984. An improved method for determining the regional stress tensor using earthquake focal mechanism data: application to the San Fernando earthquake sequence. J Geophys Res, 89: 9305–9320

Guo Q L, Wang C H, Ma H S, et al. 2009. In-situ hydro-fracture stress measurement before and after the Wenchuan M_s8.0 earthquake of China (in Chinese). Chin J Geophys, 52: 1395–1401

Hardebeck J L, Michael A J. 2006. Damped regional-scale stress inversions: Methodology and examples for southern California and the Coalinga aftershock sequence. J Geophys Res, 111: B11310

Herrmann R B, Benz H, Ammon C J. 2011. Monitoring the earthquake source process in North America. Bull Seismol Soc Amer, 101: 2609–2625

Kagan Y Y. 1991. 3-D rotation of double-couple earthquake sources. Geophys J Int, 106: 709–716

Li Z W, Xu Y, Huang R Q, et al. 2011. Crustal P-wave velocity structure of the Longmenshan region and its tectonic implications for the 2008 Wenchuan earthquake. Sci China Earth Sci, 54: 1386–1393

Li Z W, Ni S D, Hao T Y, et al. 2012. Uppermost mantle structure of the eastern margin of the Tibetan Plateau from interstation Pn traveltime difference tomography. Earth Planet Sci Lett, 335-336: 195–205

Li Z W, Tian B F, Liu S. et al. 2013. Asperity of the 2013 Lushan earthquake in the eastern margin of Tibetan Plateau from seismic tomography and aftershock relocation. Geophys J Int, 195: 2016–2022

Liu C, Zhu B J, Shi Y L. 2012. Stress accumulation of the Longmenshan Fault and recurrence interval of Wenchuan Earthquake based on viscoelasticity simulation (in Chinese). Acta Geol Sin, 86: 157–169

Luo Y, Ni S D, Zeng X F, et al. 2010. A shallow aftershock sequence in the north-eastern end of the Wenchuan earthquake aftershock zone. Sci China Earth Sci, 53: 1655–1664

Luo Y, Ni S D, Zeng X F, et al. 2011. The M5.0 Suining-Tongnan (China) earthquake of 31 January 2010: A destructive earthquake occurring in sedimentary over. Chin Sci Bull, 56: 521–525

Lu J, Wang X S, Su J R, et al. 2013. Hypocentral location and source mechanism of the M_s7.0 Lushan earthquake sequence (in Chinese). Chin J Geophys, 56: 1753–1763

McKenzie D P. 1969. The relation between fault plane solutions for earthquakes and the directions of the principal stresses. Bull Seismol Soc Amer, 59: 591–601

Michael A J. 1984. Determination of stress from slip 393 data: Faults and folds. J Geophys Res, 89: 11517–11526

Michael A J. 1987. Use of focal mechanisms to determine stress: A control study. J Geophys Res, 92: 357–368

Patton H, Zandt G. 1991. Seismic moment tensors of western U S earthquakes and implications for the tectonic stress field. J Geophys Res, 96: 18245–18259

Parsons T, Ji C, Kirby E. 2008. Stress changes from the 2008 Wenchuan earthquake and increased hazard in the Sichuan basin. Nature, 454: 509–510

Qin X H, Chen Q C, Tan C X, et al. 2013. Analysis of current geostress state and seismic risk in southwest segment of Longmenshan fracture belt (in Chinese). Chin J Rock Mech Eng , 32: 2870–2876

Romanowicz B, Dreger D, Pasyanos M, et al. 1993. Monitoring of strain release in central and northern California using broadband data. Geophys Res Lett, 20: 1643–1646

Royden L H, Burchfiel B C, van der Hilst R D. 2008. The geological evolution of the Tibetan Plateau. Science, 321: 1054

Shan B, Xiong X, Zheng Y, et al. 2009. Stress changes on major faults caused by M_w7.9 Wenchuan earthquake, May 12, 2008. Sci China Ser D-Earth Sci, 52: 593–601

Shao Z G, Zhou L Q, Jang C S, et al. 2010. The impact of Wenchuan M_s8.0 earthquake on the seismicity of surrounding faults (in Chinese). Chin J Geophys, 53: 1784–1795

Shen Z K, Lu J, Wang M, et al. 2005. Contemporary crustal deformation around the southeast borderland of the Tibetan Plateau. J Geophys Res, 110: B11409

Shi Y L, Cao J L. 2010. Some aspects in static stress change calculation-Case study on Wenchuan earthquake (in Chinese). Chin J Geophys, 53: 102–110

Shi Y T, Gao Y, Zhao C P, et al. 2009. A study of seismic anisotropy of Wenchuan earthquake sequence (in Chinese). Chin J Geophys, 52: 398–407

Shi Y T, Gao Y, Zhang Y J, et al. 2013. Shear-wave splitting in the crust in Eastern Songpan-Ganze block, Sichuan-Yunnan block, and western Sichuan Basin (in Chinese). Chin J Geophys, 56: 481–494

Toda S , Lin J, Meghraoui M, et al. 2008. 12 May 2008 M=7.9 Wenchuan, China, earthquake calculated to increase failure stress and seismicity rate on three major fault systems. Geophys Res Lett, 35: L17305

Wan Y G, Shen Z K, Sheng S Z, et al. 2009. The influence of 2008 Wenchuan earthquake on surrounding faults. Acta Seismol Sin, 31: 128–139

Wang C Y, Chang L J, Lu Z Y, et al. 2007. Seismic anisotropy of upper mantle in eastern Tibetan Plateau and related crust-mantle coupling pattern. Sci China Ser D-Earth Sci, 50: 1150–1160

Wang Y Z, Wang E N, Shen Z K, et al. 2008. GPS-constrained inversion of present-day slip rates along major faults of the Sichuan-Yunnan region, China. Sci China Ser D-Earth Sci, 51: 1267–1283

Wu Y M, Hsu Y J, Chang C H, et al. 2010. Temporal and spatial variation of stress field in Taiwan from 1991 to 2007: Insights from comprehensive first motion focal mechanism catalog. Earth Planet Sci Lett, 298: 306–316

Xie F R, Cui X F, Zhao J T, et al. 2004. Regional division of the recent tectonic stress field in China and adjacent areas (in Chinese). Chin J Geophys, 47: 654–662

Xie F S, Zhang H Y ,Cui X F, et al. 2011. The modern tectonic stress field and strong earthquakes in hina(in Chinese). Recent Dev World Seismol, 385: 4–12

Xu Z H. 2001. A present-day tectonic stress map for eastern Asia region (in Chinese). Acta Seismol Sin, 23: 492–501

Xie Z J, Jin B K, Zheng Y, et al. 2013. Source parameters inversion of the 2013 Lushan earthquake by combining teleseismic waveforms and local seismograms. Sci China Earth Sci, 56: 1177–1186

Yang X P, Jiang P, Song F M, et al.1999. The evidence of the south Longmenshan fault zones cutting late quaternry stratum (in Chinese). Seismol Geol, 21: 341–345

Zeng X F, Luo Y, Han L B, et al. 2013.The Lushan M_s7.0 earthquake on 20 April 2013: A high-angle thrust event (in Chinese). Chin J Geophys, 56: 1418–1424

Zhao L, Luo Y, Liu, T Y,et al. 2013. Earthquake focal mechanisms in Yunnan and their inference on regional stress field. Bull Seismol Soc Amer, 103: 2498–2507

Zhao L S, Helmberger D V. 1994. Source estimation from broadband regional seismograms. Bull Seismol Soc Amer, 84: 91–104

Zhan Z W, Helmberger D, Simons M, et al. 2012. Anomalously steep dips of earthquakes in the 2011 Tohoku-Oki source region and possible explanations. Earth Planet Sci Lett, 353-354: 121–133

Zhang P Z, Wen X Z, Xu X W, et al. 2009. The multiple-unit mode of the Wenchuan 8.0 great earthquake occurrence (in Chinese). Chin Sci Bull, 54: 944–953

Zhang P Z. 2013. A review on active tectonics and deep crustal processes of the western Sichuan region, eastern margin of the Tibetan Plateau. Tectonophysics, 584: 7–22

Zheng Y, Ma H S, Lu J, et al. 2009. Source mechanism of strong aftershocks ($M_s \geqslant 5.6$) of the 2008/05/12 Wenchuan earthquake and the implication for seismotectonics . Sci China Ser D-Earth Sci, 52: 739–753

Zheng Y, Ge C, Xie Z J, et al. 2013. Crustal and upper mantle structure and the deep seismogenic environment in the source regions of the Lushan earthquake and the Wenchuan earthquake. Sci China Earth Sci, 56: 1158–1168

Zhu L, Rivera L A. 2002. A note on the dynamic 440 and static displacement from a point source in multi-layered media. Geophys J Int, 148: 619–627

Zhu L P, Helmberger D V. 1996. Advancement in source estimation techniques using broadband regional seismograms. Bull Seismol Soc Amer, 86: 1634–1641

Zoback M L. 1992. First- and second-order patterns of stress in the lithosphere: The world stress map project. J Geophys Res, 97: 11703–11728